Inner belt electron decay timescales: a comparison of Van Allen Probes and DREAM3D losses following the June 2015 storm

Jeffrey M. Broll[1]; Gregory S. Cunningham[1], David M. Malaspina[2,3]; Seth G. Claudepierre[4]; Jean-François Ripoll[5,6]

[1]Los Alamos National Laboratory, Los Alamos, NM, USA
[2]Astrophysical and Planetary Sciences Department, University of Colorado, Boulder, CO, USA
[3]Laboratory for Atmospheric and Space Physics, University of Colorado, Boulder, CO, USA
[4]Department of Atmospheric and Oceanic Sciences, University of California, Los Angeles, CA, USA
[5]CEA, DAM, DIF, Arpajon, France
[6]UPS, CEA, LMCE, Bruyères-le-Châtel, France

Key Points:

- DREAM3D simulations of Earth's inner electron belt, based on Van Allen Probes observations, are carried out to evaluate model decay rates
- Pitch angle diffusion using coefficients reflecting geomagnetic activity demonstrates realistic decay rates
- Decay rates extracted with a RANSAC-based algorithm from modeled and observed fluxes agree, while theoretical lifetimes are too long

1 Abstract

NASA's Van Allen Probes observed significant, long-lived fluxes of inner belt electrons up to ∼1MeV after geomagnetic storms in March and June 2015. Reanalysis of MagEIS data with improved background correction showed a clearer picture of the relativistic electron population that persisted through 2016 and into 2017 above the Fennell et al. (2015) limit. The intensity and duration of these enhancements allow estimation of decay timescales for comparison with simulated decay rates and theoretical lifetimes.

We compare decay timescales from these data and DREAM3D simulations based on them using geomagnetic activity-dependent pitch angle diffusion coefficients derived from plasmapause-indexed wave data (Malaspina et al., 2016, 2018) and phase space densities derived from MagEIS observations. Simulated decay rates match observed decay

rates more closely than the theoretical lifetime due to significantly nonequilibrium pitch angle distributions in simulation and data. We conclude that nonequilibrium effects, rather than a missing diffusion or loss process, account for observed short decay rates.

2 Introduction

Energetic electrons stably trapped in Earth's inner magnetosphere form the (electron) radiation belts: an inner (peaking below $\sim 2R_E$) and outer (peaking $\sim 3{-}6R_E$) belt separated by a slot region (generally at $2{-}4R_E$) of lower fluxes. Inner belt fluxes have historically been observed to be relatively stable over time, with decay timescales of months to years reported for relativistic electrons (e.g. Welch Jr. et al. (1963); Van Allen (1964); Bostrom et al. (1970); West Jr. and Buck (1976)).

Radiation belt observations from NASA's Van Allen Probes (Mauk et al., 2013) provided the best available characterization of inner belt electron decays over its seven-year duration, with the Magnetic Electron Ion Spectrometer (MagEIS) detectors (Blake et al., 2013; Claudepierre et al., 2021) in particular covering inner belt energies with reduced background contamination due to the colocated proton radiation belt (Claudepierre et al., 2015).

The development of a more advanced background correction for MagEIS measurements by Claudepierre et al. (2019) quantified with greater accuracy the duration and spatial extent of inner-belt injections and enhancements at energies above 700keV above the (Fennell et al. (2015) limit of 0.1 $\mathrm{cm^{-2}s^{-1}sr^{-1}keV^{-1}}$. These reanalyzed data, referred to as "alternate-corrected" throughout this work, were used in several subsequent studies of inner belt electrons; in particular, Claudepierre et al. (2020a, 2020b) showed that observed decay timescales below $L \simeq 3.5$ are shorter than theoretical lifetimes (corresponding to the slowest-decaying mode of the pitch angle diffusion operator) and suggested that additional loss processes might be needed to explain this discrepancy. Further comparisons with event-driven simulations agreed qualitatively with these timescales above $L = 3.5$ (Ripoll et al., 2017, 2019), but wave properties there differ significantly from those in the inner belt and the relevant characteristics in Ripoll et al. (2019) are not seen at low L.

This work examines inner belt electron decay timescales inferred from observations and DREAM3D radiation belt simulations (Tu et al., 2013, 2014; Cunningham et al.,

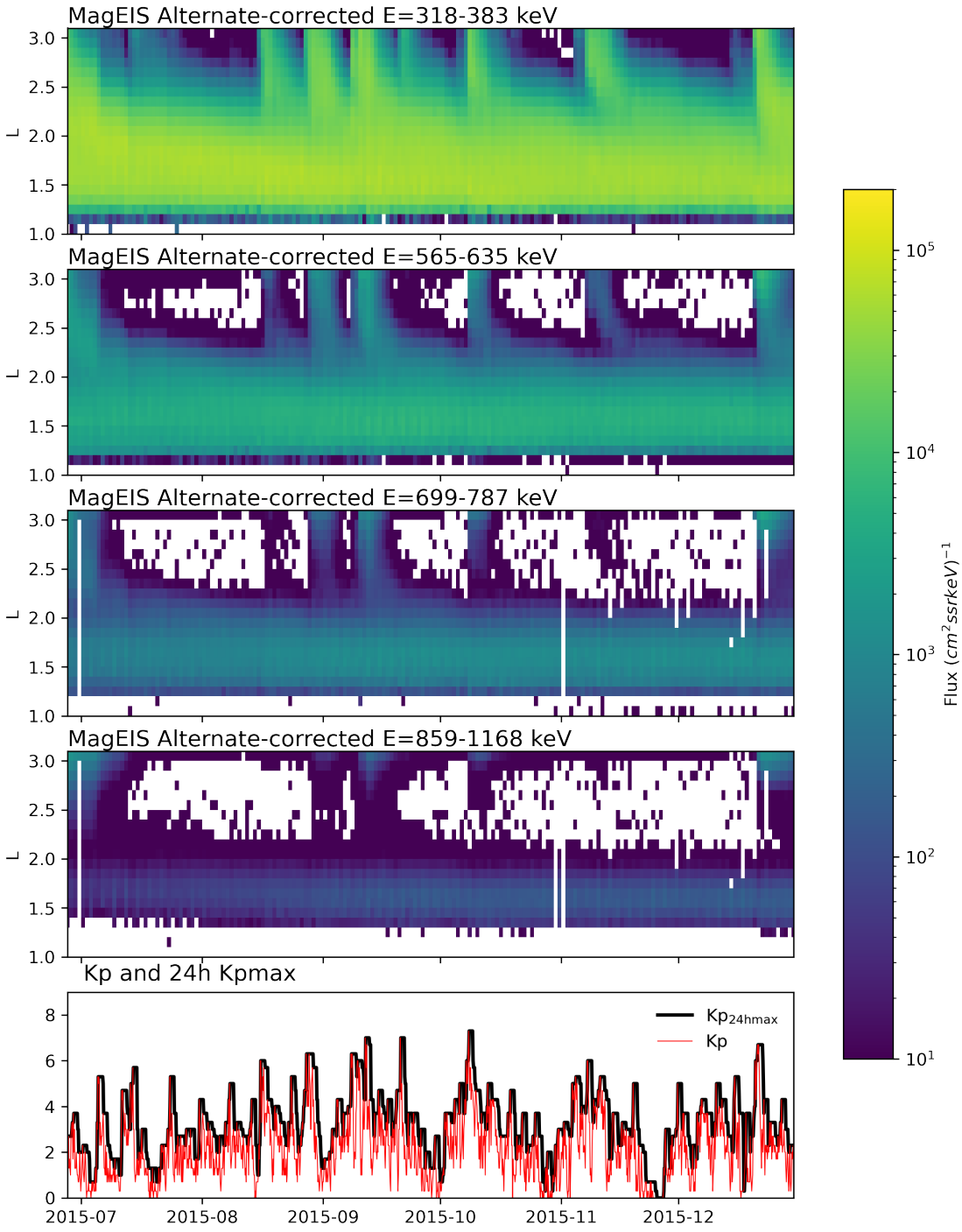

Figure 1. MagEIS electron L-time spectra and Kp geomagnetic activity index from 1 June 2015 to 31 Dec 2015. The radial diffusion in the simulation is modulated by Kp at the original 3-hour cadence. $Kp^{\star}$, the maximum Kp over the previous 24 hours, is used to calculate plasmapause location, which controls the pitch-angle diffusion coefficients used in the simulation.

2018). A long-lived flux enhancement, which followed storm activity in late June 2015 and continued into 2017, provides an opportunity to test predictions and models over a long period of slow decay. Figure 1 shows MagEIS fluxes at selected energies for L≤ 3, along with 3h and 24h-max Kp data, following this enhancement in June through the end of 2015, in which several smaller injections are seen throughout the interval. The simulation in this study follows the injections and decays displayed in the figure.

3 DREAM3D simulation of 2015 inner belt injection and decay

The DREAM3D radiation belt model solves the Fokker-Planck equation (cf. e.g. Schulz and Lanzerotti (1974)) in three dimensions by splitting the diffusion operator into radial and $\alpha-p$ diffusion components, alternating between the two to calculate 3D diffusion (cf. Tu et al. (2013) for a detailed description of the model). The distribution function is resampled between the (p, α, L, t) and (μ, K, L, t) grids at the radial diffusion timesteps, and the 12 hour radial diffusion timestep is long enough to ensure that the resampling does not introduce problematic numerical diffusion. In this work the simulation included radial diffusion, pitch angle diffusion by wave activity, and Coulomb collision-induced pitch angle scattering and energy loss.

Here and throughout this work α is equatorial pitch angle, p is momentum, L is the Roederer L^* (where the asterisk is dropped throughout), and $T(\alpha) \simeq 1.38-0.32\left(\sin\alpha + \sqrt{\sin\alpha}\right)$ is the approximate normalized dipole bounce period.

3.1 Radial diffusion

$$\frac{\partial f\left(\mu, K, L, t\right)}{\partial t} = L^2 \frac{\partial}{\partial L} L^- 2 \left(D_{LL} \frac{\partial f\left(\mu, K, L, t\right)}{\partial L} \right) \tag{1}$$

is solved by implicit finite differencing using user-specified radial diffusion coefficients. The phase space distribution $f(\mu, K, L, t)$ is expressed in terms of adiabatic invariant coordinates: magnetic moment $\mu = p_\perp^2 / 2m_0 B$, bounce parameter $K = \int_{s_m}^{s'_m} \sqrt{B_m - B(s)} ds$ (where the integral is taken along the field line between two mirror points s_m, s'_m where the magnetic field strength is B_m), and L. The Kp-dependent combined electric and magnetic D_{LL} of Brautigam and Albert (2000) is used (cf. Drozdov et al. (2021) for comparisons between radial diffusion coefficients).Radial diffusion is calculated on a $100\times 400 \times 300$ mesh in L, μ, K described in the Supplementary Information.

Radial diffusion from a time-dependent outer boundary at $L = 3.025$ provides flux injections, and the inner radial boundary condition is $f = 0$ at $L = 1.025$.

A radial diffusion timestep of 12 hours is used after the first simulated day. A timestep of 90 minutes is used on the first simulated day in order to examine the early evolution of the pitch angle distributions (PADs), but this component is not presented or analyzed here.

3.2 Pitch angle diffusion due to wave activity

$$\frac{\partial f(p,\alpha,L,t)}{\partial t} = (T(\alpha)\sin 2\alpha)^{-1}\,\frac{\partial}{\partial \alpha}\left(T(\alpha)\sin 2\alpha D_{\alpha\alpha}\frac{\partial f(p,\alpha,L,t)}{\partial \alpha}\right) \tag{2}$$

is solved for each L independently using the Crank-Nicholson method on a grid with

360 α bins linearly spaced in $[0, \pi/2]$ and
100 momentum bins linearly spaced in $[0.335, 3.474]$ MeV/c

where the momentum boundaries correspond to electron energies 100 keV and 3 MeV respectively.

Mixed and momentum diffusion terms were not expected to be significant and were thus omitted. Pitch angle boundary conditions are $\frac{\partial f}{\partial \alpha}(\pi/2) = 0$ and $f(0) = 0$. The pitch angle diffusion timestep is 15 seconds throughout the simulation.

Pitch angle diffusion coefficients from lightning-generated whistler (LGW) and hiss waves are calculated using a database of wave power sorted by plasmapause location L_{PP} and plasmapause distance $dL_{PP} = L - L_{PP}$ (Malaspina et al., 2016) from the Van Allen Probes EMFISIS search coil magnetometer (Kletzing et al., 2013). The data are sorted into 4 bins in L_{PP}, 50 bins in dL_{PP}, 4 bins in magnetic local time MLT, and 65 bins in frequency f to obtain a distribution of power in frequency at each L_{PP}, dL_{PP}, MLT. The L_{PP} sorting is an important feature based on a key recognition of the dependence of the hiss wave power on electron density (Malaspina et al., 2016, 2018).

Separately, distributions of power in wave normal angle θ for hiss and for LGWs are calculated at each L_{PP}, dL_{PP}, MLT, using the method of Santolík et al. (2003) to obtain θ for each sample and weighing samples according to their power. The resulting

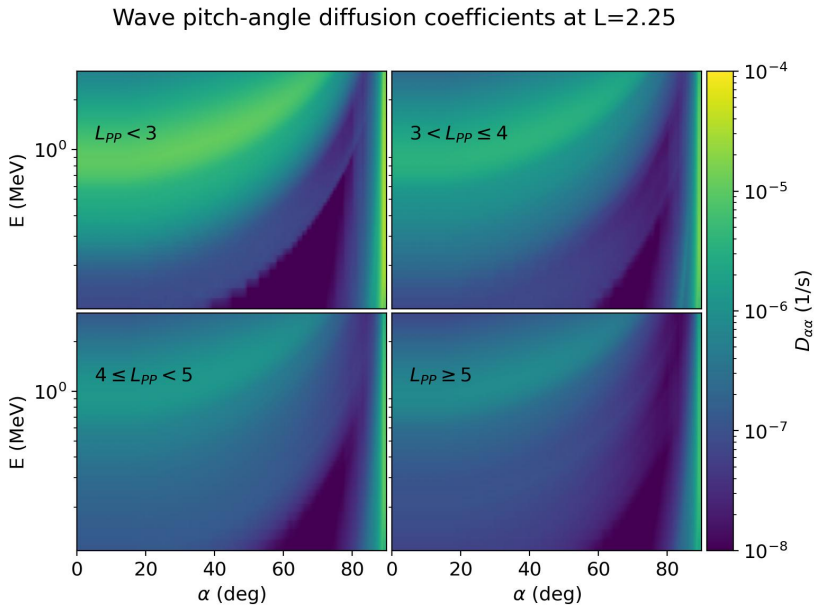

Figure 2. Diffusion coefficients for LGW and hiss waves at $L = 2.25$ vs. pitch angle and energy, as obtained from EMFISIS data as described in Section 3.2.

θ distribution is weighted by *power*, rather than *occurrence*; (Li et al., 2016) discusses this difference.

The product of the wave power distributions over frequency and wave normal angle provides a distribution of wave power over frequency and wave normal angle at each L_{PP}, dL_{PP}, MLT, which is then averaged over MLT. This distribution is assumed to apply at all magnetic latitudes. The method of Glauert and Horne (2005) is used to obtain diffusion coefficients from this distribution, using the cold plasma density model of (Ozhogin et al., 2012) and a dipole magnetic field. This yields diffusion coefficients in L, α, p for each L_{PP} bin, which allows DREAM3D to vary diffusion coefficients according to geomagnetic activity; cf. Figure 2. Further details are included in the Supplementary Information.

Diffusion coefficients from hiss and LGW waves are calculated at each radial diffusion timestep by averaging the L_{PP}-indexed diffusion coefficients according to their L_{PP}'s occurrence in that timestep. L_{PP} is calculated from 3-hour Kp data interpolated linearly to 1-minute cadence and an L_{PP} bin is assigned to each 1-minute interval by

the Carpenter and Anderson (1992) relation $L_{PP} = 5.6 - 0.46Kp^{\star}$. The pitch angle diffusion coefficients in that radial diffusion timestep are then calculated by averaging the four L_{PP}-indexed diffusion coefficients with weights given by the fraction of the radial diffusion timestep that L_{PP} occupied their L_{PP} bins. This L_{PP} binning accounts for geomagnetic activity without the need for an additional geomagnetic index dependence. Calculations involving L_{PP} assume the largest value consistent with the L_{PP} bin.

3.3 Pitch angle scattering and energy loss due to Coulomb collisions

The effects of Coulomb collisions at low $L-$shells are calculated as in Selesnick (2012) and Cunningham et al. (2018); the latter also discusses how pitch-angle scattering and energy loss due to collisions are calculated in DREAM3D. Collision calculations employ the NRLMSISE-00 neutral atmosphere (Picone et al., 2002) and IRI-2012 ionosphere (Bilitza et al., 2014) models.

3.4 Initial condition

In order to reproduce PADs for the post-storm period, we combine daily-averaged PADs with $\Delta\alpha = 5^{\circ}$ at MagEIS energies from standard-corrected, unbinned MagEIS data from all four electron spectrometers and the "alternate-corrected" data from Claudepierre et al. (2019). For energies and L-shells where alternate-corrected data from Claudepierre et al. (2019) are available, the alternate-corrected fluxes j_{alt} are combined with the standard-corrected MagEIS PADs $j_{std}(\alpha)$:

$$
\begin{aligned}
j(\alpha) &= j_{alt}^{B(\cos\alpha)} \cdot j_{std}(\alpha)^{1-B(\cos\alpha)}, \quad \text{where} \\
B(x) &= 0, && x \geq \cos(50^{\circ}), \\
&= \exp\left(1 - \frac{x^2}{\cos(50^{\circ})^2 - x^2}\right), && 0 \leq x < \cos(50^{\circ})
\end{aligned}
\tag{3}
$$

At high energies where measurements suffered from low count rates, a power law in energy is calculated from alternate-corrected data from energy channels above 470keV and the PAD from the highest energy with good counting statistics is cloned at higher energies with the estimated power law scaling.

The resulting $j\,(\alpha, E)$ are then extended to cover all simulated pitch angles and energies. For each L, $\log(j)$ is interpolated linearly in $(\log(E), \sin\alpha)$ and nearest-neighbor

extrapolated to the edges of the $(\log(E), \sin\alpha)$ plane. This extrapolated distribution is then converted to a simulation-gridded phase space density $f = 3.32{\cdot}10^{-8} j/p^2c^2$ (Chen et al., 2006).

3.5 Boundary condition

A boundary condition is constructed for each simulation day at $L = 3.025$ using the same daily-averaged PADs used for the initial condition. As alternate-corrected data are not produced for $L > 3$, only the standard-corrected data are used. When an energy channel has very low and sparse flux, all of its data are removed from the interpolation step; this was not necessary for the initial condition.

Figure 3 shows simulated and observed fluxes at ~ 600 keV and at ~ 1 MeV. The simulation reproduces the timing of injections from high L-shells well. Reproducing the absolute flux level after each injection is not necessary to study loss timescales and is outside the scope of this work.

4 Decay timescales in (L, E) in data and simulations

To evaluate DREAM3D loss modeling, we compare decay timescales extracted from simulations and from alternate-corrected MagEIS data by outlier-robust fitting of $\log(j(t))$ to degree 1 in t at fixed E and L. As the alternate-corrected data are limited to one pitch angle sample covering roughly equatorial pitch angles above 70°, DREAM3D fluxes are averaged over $\alpha \geq 70$ to obtain a comparable quantity for fitting. Results are not particularly sensitive to variations in the simulation pitch angle threshold, likely because the decay rate is controlled by the diffusion minimum located between the Landau resonance and the first cyclotron resonance and because this minimum is located at high pitch angles within $[70, 90]^\circ$ for these L-shells and energies (Mourenas & Ripoll, 2012).

We also calculate the theoretical lifetimes by determining the slowest decay rate under wave and Coulomb pitch angle scattering, as in equations (12) and (13) of Lyons et al. (1972).

4.1 Extracting decay timescales with Random Sample Consensus

Decay timescales are extracted from intervals of decreasing flux using an approach based on Random Sample Consensus (RANSAC) (Fischler & Bolles, 1981), an outlier-

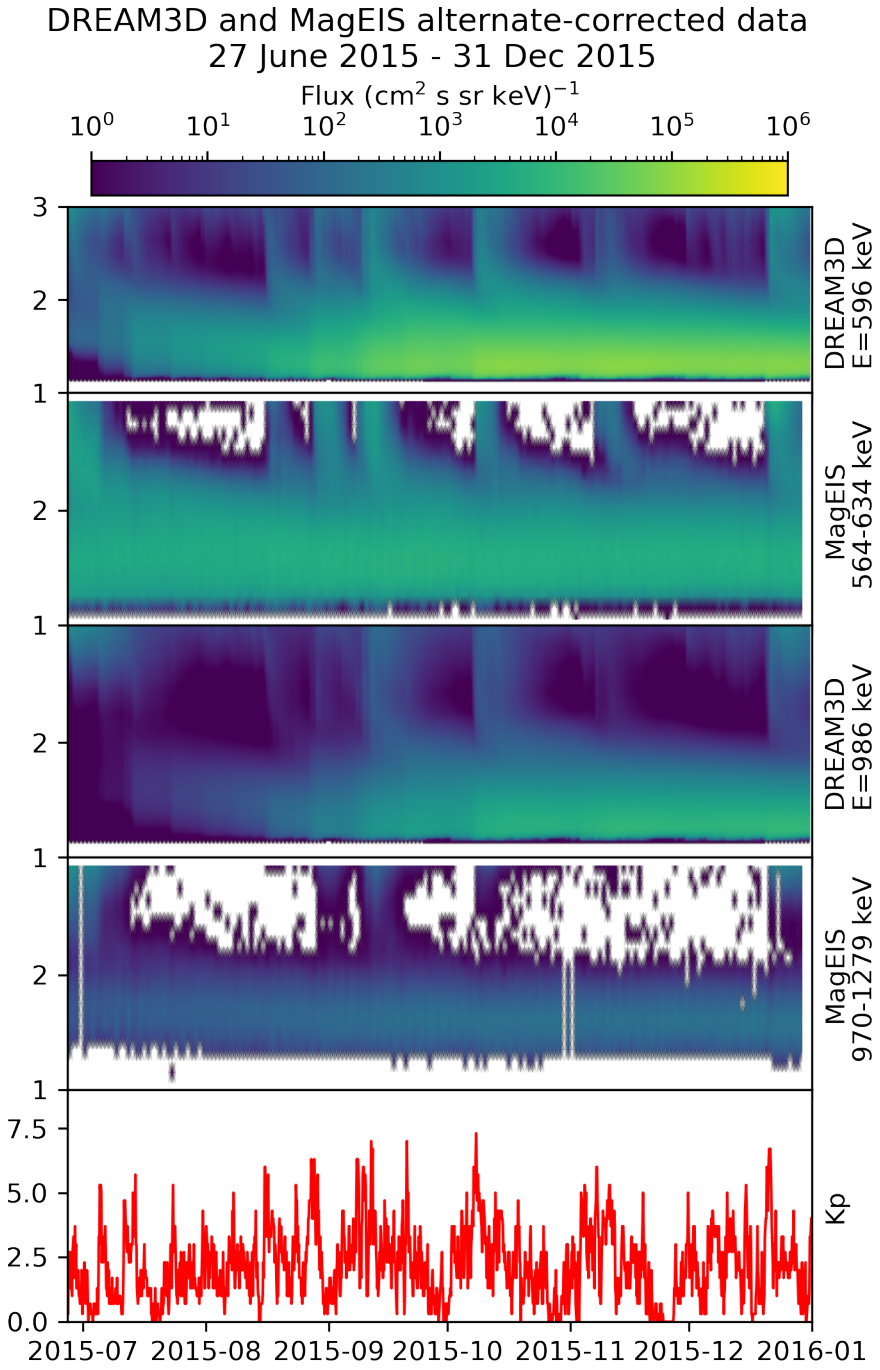

Figure 3. DREAM3D and MagEIS fluxes near 90° at 600 keV and 1 MeV show that injections from the outer boundary are reproduced by Kp-dependent radial diffusion.

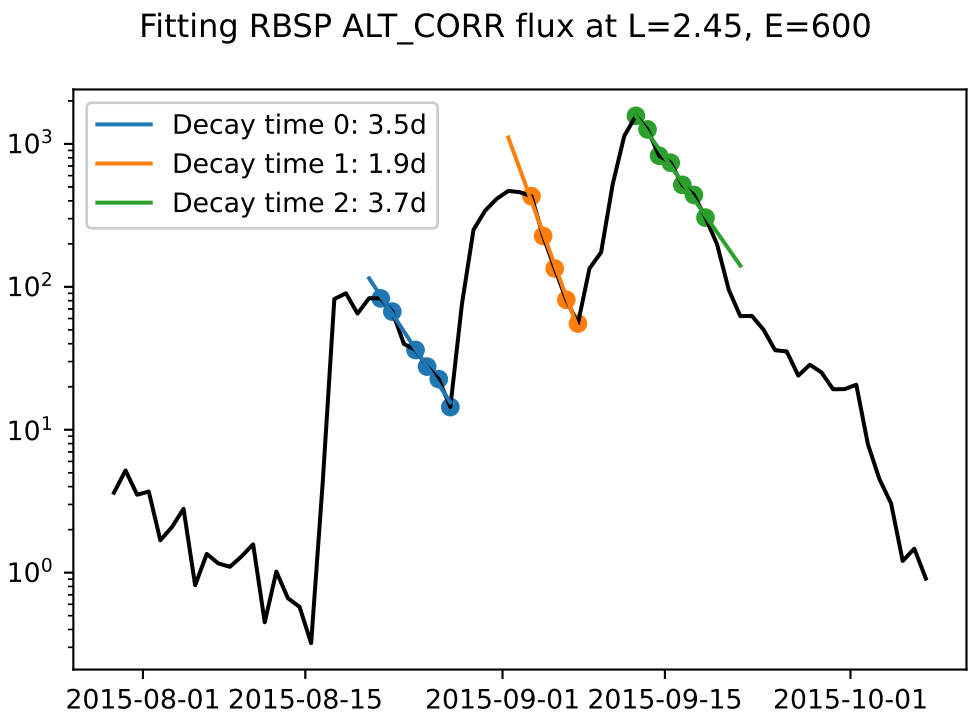

Figure 4. Example RANSAC decay time extraction from Van Allen Probes data. Time windows where flux decreases are identified and a fit of $\log(j)$ to t is obtained by RANSAC. This is repeated for each window of decreasing flux, for each energy, and for each L-shell, and decay timescales are obtained from each fit of sufficient quality and length. Note that in the third fit the method excludes the period of brief increase in the decay rate after the fit interval, which would erroneously increase the decay rate, even though the flux continued to decrease.

184 robust model fitting algorithm. RANSAC iteratively attempts to fit random subsamples
185 of data to a model, categorize subsample elements as inliers or outliers, expand the sub-
186 sample, and refit the model until sample size cannot be increased and quality cannot be
187 improved.

188 In order to extract multiple decay timescales from a timeseries this procedure can
189 be iterated for each window of decreasing flux. This procedure is repeated for each en-
190 ergy and each L-shell, for both simulation data and the alternate-corrected MAGEIS data,
191 yielding a database of intervals of decay intervals and their decay rates. Figure 4 shows
192 three fits to MagEIS observations of 600keV electrons at $L = 2.45$.

Similar results have been obtained previously, most notably in the work of Claudepierre et al. (2020b) where decay windows are identified in smoothed fluxes, decay window fluxes are fit to exponentials, and thresholds on correlation coefficient and percent error ensured that only good fits are utilized. The fits here are maximized subject to the outlier threshold and minimum window length, which are set at squared error 0.01 and at least 5 days, respectively.

4.2 Comparison of simulated and observed decay timescales

Figure 5 summarizes the decay timescales extracted from the entire Van Allen Probes duration, the decay timescales extracted from the DREAM3D simulation, and consistent theoretical lifetimes predicted from the slowest decaying mode of the pitch angle diffusion operator. For data and simulation, median and average are taken over the set of extracted timescales without weighting by time. For the theoretical lifetimes we take the median and average of the lifetimes calculated in a consistent manner from each L_{PP} bin's diffusion coefficients. The minimum, median, average and maximum decay timescales and lifetimes are plotted for all simulated energy and L in the top left of the figure, and the median timescales at ~ 600 keV are plotted in the bottom right of the figure.

The DREAM3D decay timescales are much closer to the observed decay timescales than the theoretical lifetimes - an improvement of over an order of magnitude is found across much of the simulated energy range at low L. We attribute this agreement to PADs that are far from the "equilibrium" distribution shape associated with the slowest-decaying mode of the pitch angle diffusion operator (cf. Ripoll et al. (2015); Loridan et al. (2017); Millan et al. (2021)). Separating this section

4.3 Equilibrium lifetimes are inappropriate when equilibrium is unreachable

Radiation belt populations are conventionally assumed to settle rapidly into the equilibrium PAD. The slowest decay rate would determine the dominant decay timescale in this scenario, even if flux injections produced distributions departing significantly from equilibrium, as the settling-in period, which is comparable to the second-slowest decay timescale (Shprits et al., 2006), would be short compared to the equilibrium decay timescale.

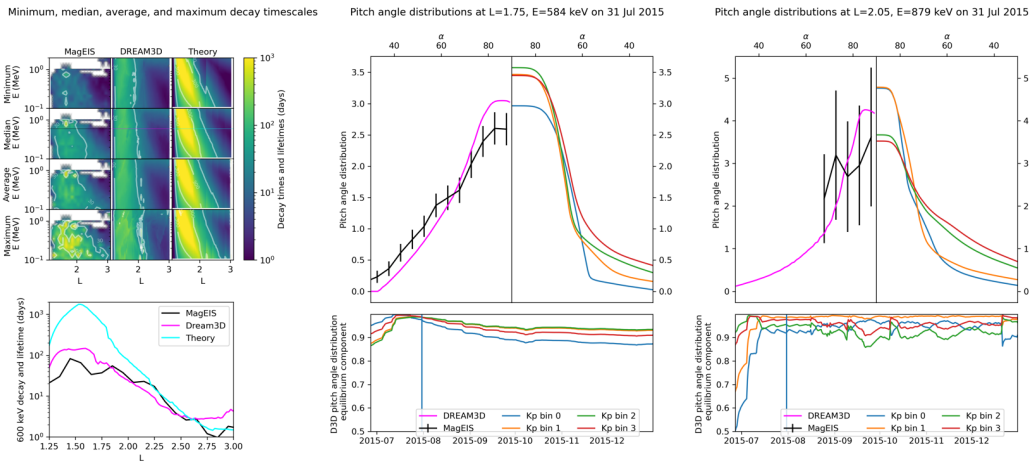

Figure 5. Observations and simulations both exhibit decay timescales significantly shorter than the predicted lifetimes and nonequilibrium PADs, suggesting that nonequilibrium effects are responsible for the observed decay timescales.

(Left) Decay timescales were calculated from MagEIS alternate-corrected fluxes and DREAM3D fluxes averaged over $\alpha_{eq} \in [70°, 90°]$ and compared with the expected lifetimes from each Kp bin's pitch-angle diffusion coefficients. Theoretical lifetimes are longer than observed decay timescales at low L. DREAM3D with time-dependent diffusion coefficients produces decay timescales closer to those observed in MagEIS data over much of the inner belt L and energy range (top); comparison at $E \simeq 600keV$ (indicated by colored lines in the top) shows an improvement by a factor of ∼10 (bottom).

(Middle) Observed (black) and simulated (magenta) PADs are compared with theoretical equilibrium distributions (top, with Kp bin i shifted by $i/8$ to reduce overlap) for ∼ 600 keV electrons at $L = 1.75$. The simulated distributions' equilibrium components (bottom) do not remain at 1 for much of the interval - contradicting the conventional assumption of a steady "settling-in" to a slowest-decaying eigenmode and subsequent decay according to its eigenvalue, each Kp bin has its own equilibrium distribution and the simulation distribution does not converge to any of them.

(Right) Similar to middle, but for ∼ 900keV electrons at $L = 2.05$. Sharp, near-vertical slopes are seen throughout the interval, indicating a rapid approach (increasing slope) or departure (decreasing slope) of the simulated distribution towards the corresponding equilibrium distribution.

This assumption is invalid when pitch-angle diffusion exhibits time-varying behavior. Different diffusion operators need not share eigenmodes, and in particular an eigenmode before a change need not remain an eigenmode after the change. The concept of "settling into the equilibrium distribution" is thus inappropriate here because the underlying equilibrium is changing faster than it can be reached. Real distributions will then generally have significant components in faster-decaying eigenmodes, and thus an enhanced decay rate.

Observed, simulated, and theoretical equilibrium PADs are compared in the top middle and top right of Figure 5. The inner products of the four Kp bins' equilibrium PAD and the DREAM3D PAD are shown in the bottom middle and bottom right, The last quantity is calculated for each DREAM3D PAD by normalizing the DREAM3D distribution and taking its inner product with each equilibrium distribution, where the inner product and norm for the pitch-angle diffusion equation are

$$< f, g >= \int_{LC}^{90^\circ} f(\alpha)\ g(\alpha)\ T(\alpha) \sin(2\alpha)\ d\alpha, \quad |f| = \sqrt{< f, f >} \qquad (\star)$$

(cf. e.g. chapter V of Courant and Hilbert (1953), chapter 8 of Arfken et al. (2013)). The timeseries plots depict $\langle f_{\mathrm{DREAM3D}}, f_{\mathrm{equilibrium}} \rangle$ where $|f_{\mathrm{DREAM3D}}| = |f_{\mathrm{equilibrium}}| = 1$ so departure from equilibrium is indicated by values below 1.

For a distribution settling into equilibrium, such a timeseries would approach 1 rapidly. This is seen in the initial period in both timeseries, but the majority of the simulated interval is seen to exhibit nonequilibrium distributions, and the failure to asymptotically approach 1 indicates that the nonequilibrium is being actively maintained throughout that time. This suggests that the real decay rate is augmented by persistent presence of flux in faster-decaying modes due to the nonconstant equilibrium.

We suggest that this obviates the need for a "missing" scattering process to bring theoretical lifetimes in line with observations, as raised in (Claudepierre et al., 2020a) and elsewhere. The failure of this assumption has also been addressed for scattering in plumes in (Millan et al., 2021), and the effects of time-dependent equilibria will be the subject of more thorough investigation in an upcoming work.

5 Summary

We have carried out a DREAM3D simulation of the Earth's inner electron radiation belt based on several months of a period where Van Allen Probes observations indicated enhanced fluxes up to ~ 1 MeV in order to evaluate DREAM3D's ability to model inner belt electron losses. The simulation used initial and boundary conditions generated from MagEIS data, employing data from all four MagEIS detectors on both Van Allen Probes spacecraft and merging alternatively-corrected fluxes for near-equatorially-mirroring electrons. Electron injections from the boundary and pitch angle diffusion coefficients generated from dynamic EMFISIS wave data both induced geomagnetic activity-driven changes in the inner belt.

Decay timescales are extracted automatically using an outlier-robust algorithm to fit periods of decaying flux. Decay timescales obtained from DREAM3D simulations compare favorably with timescales extracted from the Van Allen Probes MagEIS measurements, with an order-of-magnitude improvement in regions of strongest disagreement between theoretical and observed decay rates.

This agreement is attributed to persistent nonequilibrium effects due to the use of geomagnetic activity-dependent pitch-angle diffusion. The changes in the pitch-angle diffusion refill faster-decaying modes and enhance decay well beyond the theoretical lifetime obtained by considering only the decay rate of the slowest-decaying eigenmode. We conclude that nonequilibrium effects account for much of the discrepancy between theoretical and observed decay rates for inner belt electrons and that this effect, rather than a missing diffusion or process, suffices to explain observed decay rates.

6 Future work

This work was undertaken in support of efforts to model radiation belt remediation (cf. e.g. Delzanno et al. (2020)), and the impact of nonequilibrium effects on such a scheme are far from fully explored - for example, reshaping distributions to maximize the flux in higher eigenmodes may prove more effective than allocating the same power towards enhancing the equilibrium decay rate. This, and other studies, would also benefit from adapting DREAM3D to use more generalized grids in energy and pitch angle than those used here, such as logarithmic energy steps and nonlinear α grids more concentrated around the loss cone.

The use of truncated eigenmode expansions, rather than pitch-angle grids, could also yield more efficient high-fidelity simulations and computationally feasible ensemble studies in situations where pitch angle diffusion is dominant; this is being explored along with other consequences of Sturm-Liouville theory and possible generalizations to diffusion with momentum and mixed terms included.

While mixed and momentum terms were not expected to be important, the procedure described for calculating pitch angle diffusion coefficients can also be carried out to produce mixed and momentum diffusion coefficients; however, the analysis carried out to compare PADs and equilibria would not translate directly without a more general Sturm-Liouville theory for higher-dimensional problems.

Finally, other pitch angle scattering sources, such as those from ground-based VLF transmitters or space-based remediation missions, could be modeled and included if they are suspected - or hoped - to be significant. At the time of this work there were not satisfactory models of these two sources.

7 Acknowledgments

The authors thank the International Space Sciences Institute (ISSI) and the participants in a 2020 ISSI workshop, during which this work was begun.

JB and GC are supported by the Laboratory Directed Research and Development program of Los Alamos National Laboratory under project 20200073DR.

The work by GC and JFR was performed under the auspices of an agreement between CEA/DAM and NNSA/DP in cooperation on fundamental science.

We acknowledge the use of high performance computing through the LANL Institutional Computing project to perform the DREAM3D simulations for this work.

We acknowledge support from Defense Threat Reduction Agency under Project Nos. DTRA1308134079 and DTRA1138125 for the development of DREAM3D.

We also wish to thank Mike Henderson, creator of the LanlGeoMag software library that was used to trace field lines and compute drift shells for this article, for assistance with using the library.

8 Open Research

MagEIS data are publicly available at the RBSP-ECT SOC, which is now accessible at `rbsp-ect.newmexicoconsortium.org/rbsp_ect.php`.

Van Allen Probes and OMNI data are analyzed with SpacePy (Morley et al., 2021). The lifetime analysis borrowed extensively from the scikit-learn (Pedregosa et al., 2011) implementation of the RANSAC algorithm. Extensive use was made of GNU Parallel (Tange, 2018).

References

Arfken, G. B., Weber, H.-J., & Harris, F. E. (2013). *Mathematical methods for physicists: a comprehensive guide* (7th ed ed.). Amsterdam ; Boston: Elsevier.

Bilitza, D., Altadill, D., Zhang, Y., Mertens, C., Truhlik, V., Richards, P., ... Reinisch, B. (2014). The International Reference Ionosphere 2012 – a model of international collaboration. *Journal of Space Weather and Space Climate*, *4*, A07. Retrieved from `http://www.swsc-journal.org/10.1051/swsc/2014004` doi: 10.1051/swsc/2014004

Blake, J. B., Carranza, P. A., Claudepierre, S. G., Clemmons, J. H., Crain, W. R., Dotan, Y., ... Zakrzewski, M. P. (2013, November). The Magnetic Electron Ion Spectrometer (MagEIS) Instruments Aboard the Radiation Belt Storm Probes (RBSP) Spacecraft. *Space Science Reviews*, *179*(1-4), 383–421. Retrieved from `http://link.springer.com/10.1007/s11214-013-9991-8` doi: 10.1007/s11214-013-9991-8

Bostrom, C. O., Beall, D. S., & Armstrong, J. C. (1970). Time history of the inner radiation zone, October 1963 to December 1968. *Journal of Geophysical Research (1896-1977)*, *75*(7), 1246–1256. Retrieved from `https://onlinelibrary.wiley.com/doi/abs/10.1029/JA075i007p01246` doi: 10.1029/JA075i007p01246

Brautigam, D. H., & Albert, J. M. (2000, January). Radial diffusion analysis of outer radiation belt electrons during the October 9, 1990, magnetic storm. *Journal of Geophysical Research: Space Physics*, *105*(A1), 291–309. Retrieved from `http://doi.wiley.com/10.1029/1999JA900344` doi: 10.1029/1999JA900344

Carpenter, D. L., & Anderson, R. R. (1992). An ISEE/whistler model of equatorial electron density in the magnetosphere. *Journal of Geophysical Research: Space Physics*, *97*(A2), 1097–1108. Retrieved from https://onlinelibrary.wiley.com/doi/abs/10.1029/91JA01548 doi: 10.1029/91JA01548

Chen, Y., Friedel, R. H. W., & Reeves, G. D. (2006). Phase space density distributions of energetic electrons in the outer radiation belt during two geospace environment modeling inner magnetosphere/storms selected storms. *Journal of Geophysical Research: Space Physics*, *111*(A11). Retrieved from https://agupubs.onlinelibrary.wiley.com/doi/abs/10.1029/2006JA011703 doi: https://doi.org/10.1029/2006JA011703

Claudepierre, S. G., Blake, J. B., Boyd, A. J., Clemmons, J. H., Fennell, J. F., Gabrielse, C., ... Turner, D. L. (2021, December). The Magnetic Electron Ion Spectrometer: A Review of On-Orbit Sensor Performance, Data, Operations, and Science. *Space Science Reviews*, *217*(8), 80. Retrieved from https://link.springer.com/10.1007/s11214-021-00855-2 doi: 10.1007/s11214-021-00855-2

Claudepierre, S. G., Ma, Q., Bortnik, J., O'Brien, T. P., Fennell, J. F., & Blake, J. B. (2020a). Empirically Estimated Electron Lifetimes in the Earth's Radiation Belts: Comparison With Theory. *Geophysical Research Letters*, *47*(3), e2019GL086056. Retrieved from https://onlinelibrary.wiley.com/doi/abs/10.1029/2019GL086056 doi: 10.1029/2019GL086056

Claudepierre, S. G., Ma, Q., Bortnik, J., O'Brien, T. P., Fennell, J. F., & Blake, J. B. (2020b). Empirically Estimated Electron Lifetimes in the Earth's Radiation Belts: Van Allen Probe Observations. *Geophysical Research Letters*, *47*(3), e2019GL086053. Retrieved from https://onlinelibrary.wiley.com/doi/abs/10.1029/2019GL086053 doi: 10.1029/2019GL086053

Claudepierre, S. G., O'Brien, T. P., Blake, J. B., Fennell, J. F., Roeder, J. L., Clemmons, J. H., ... Larsen, B. A. (2015, July). A background correction algorithm for Van Allen Probes MagEIS electron flux measurements. *Journal of Geophysical Research: Space Physics*, *120*(7), 5703–5727. Retrieved from https://onlinelibrary.wiley.com/doi/10.1002/2015JA021171 doi: 10.1002/2015JA021171

Claudepierre, S. G., O'Brien, T. P., Looper, M. D., Blake, J. B., Fennell, J. F.,

366 Roeder, J. L., ... Spence, H. E. (2019, February). A Revised Look at Rela-
367 tivistic Electrons in the Earth's Inner Radiation Zone and Slot Region. *Jour-*
368 *nal of Geophysical Research: Space Physics*, *124*(2), 934–951. Retrieved from
369 https://onlinelibrary.wiley.com/doi/abs/10.1029/2018JA026349 doi:
370 10.1029/2018JA026349

371 Courant, R., & Hilbert, D. (1953). *Methods of mathematical physics. Vol.1* (Vol. 1).
372 Weinheim: Interscience Publishers.

373 Cunningham, G. S., Loridan, V., Ripoll, J., & Schulz, M. (2018, April). Neoclassi-
374 cal Diffusion of Radiation-Belt Electrons Across Very Low L -Shells. *Journal*
375 *of Geophysical Research: Space Physics*, *123*(4), 2884–2901. Retrieved from
376 https://onlinelibrary.wiley.com/doi/10.1002/2017JA024931 doi:
377 10.1002/2017JA024931

378 Delzanno, G. L., Borovsky, J. E., & Mishin, E. V. (Eds.). (2020). *Active Ex-*
379 *periments in Space: Past, Present, and Future.* Frontiers Media SA. Re-
380 trieved from https://www.frontiersin.org/research-topics/7937/
381 active-experiments-in-space-past-present-and-future doi: 10.3389/
382 978-2-88963-659-4

383 Drozdov, A. Y., Allison, H. J., Shprits, Y. Y., Elkington, S. R., & Aseev, N. A.
384 (2021, August). A Comparison of Radial Diffusion Coefficients in 1-D and
385 3-D Long-Term Radiation Belt Simulations. *Journal of Geophysical Research:*
386 *Space Physics*, *126*(8). Retrieved from https://onlinelibrary.wiley.com/
387 doi/10.1029/2020JA028707 doi: 10.1029/2020JA028707

388 Fennell, J. F., Claudepierre, S. G., Blake, J. B., O'Brien, T. P., Clemmons, J. H.,
389 Baker, D. N., ... Reeves, G. D. (2015, March). Van Allen Probes show
390 that the inner radiation zone contains no MeV electrons: ECT/MagEIS
391 data. *Geophysical Research Letters*, *42*(5), 1283–1289. Retrieved from
392 https://onlinelibrary.wiley.com/doi/abs/10.1002/2014GL062874 doi:
393 10.1002/2014GL062874

394 Fischler, M. A., & Bolles, R. C. (1981, June). Random sample consensus: a
395 paradigm for model fitting with applications to image analysis and auto-
396 mated cartography. *Communications of the ACM*, *24*(6), 381–395. Re-
397 trieved from https://dl.acm.org/doi/10.1145/358669.358692 doi:
398 10.1145/358669.358692

Glauert, S. A., & Horne, R. B. (2005, April). Calculation of pitch angle and energy diffusion coefficients with the PADIE code: PADIE DIFFUSION CODE. *Journal of Geophysical Research: Space Physics*, *110*(A4). Retrieved from http://doi.wiley.com/10.1029/2004JA010851 doi: 10.1029/2004JA010851

Kletzing, C. A., Kurth, W. S., Acuna, M., MacDowall, R. J., Torbert, R. B., Averkamp, T., ... Tyler, J. (2013, November). The Electric and Magnetic Field Instrument Suite and Integrated Science (EMFISIS) on RBSP. *Space Science Reviews*, *179*(1-4), 127–181. Retrieved from http://link.springer.com/10.1007/s11214-013-9993-6 doi: 10.1007/s11214-013-9993-6

Li, W., Santolik, O., Bortnik, J., Thorne, R. M., Kletzing, C. A., Kurth, W. S., & Hospodarsky, G. B. (2016, May). New chorus wave properties near the equator from Van Allen Probes wave observation s. *Geophysical Research Letters*, *43*(10), 4725–4735. Retrieved from https://onlinelibrary.wiley.com/doi/10.1002/2016GL068780 doi: 10.1002/2016GL068780

Loridan, V., Ripoll, J.-F., & de Vuyst, F. (2017). The analytical solution of the transient radial diffusion equation with a nonuniform loss term. *Journal of Geophysical Research: Space Physics*, *122*(6), 5979-6006. Retrieved from https://agupubs.onlinelibrary.wiley.com/doi/abs/10.1002/2017JA023868 doi: https://doi.org/10.1002/2017JA023868

Lyons, L. R., Thorne, R. M., & Kennel, C. F. (1972, July). Pitch-angle diffusion of radiation belt electrons within the plasmasphere. *Journal of Geophysical Research*, *77*(19), 3455–3474. Retrieved from http://doi.wiley.com/10.1029/JA077i019p03455 doi: 10.1029/JA077i019p03455

Malaspina, D. M., Jaynes, A. N., Boulé, C., Bortnik, J., Thaller, S. A., Ergun, R. E., ... Wygant, J. R. (2016, August). The distribution of plasmaspheric hiss wave power with respect to plasmapause location: PLASMAPAUSE-SORTED HISS. *Geophysical Research Letters*, *43*(15), 7878–7886. Retrieved from http://doi.wiley.com/10.1002/2016GL069982 doi: 10.1002/2016GL069982

Malaspina, D. M., Ripoll, J., Chu, X., Hospodarsky, G., & Wygant, J. (2018, September). Variation in Plasmaspheric Hiss Wave Power With Plasma Density. *Geophysical Research Letters*, *45*(18), 9417–9426. Retrieved from https://onlinelibrary.wiley.com/doi/10.1029/2018GL078564 doi:

10.1029/2018GL078564

Mauk, B. H., Fox, N. J., Kanekal, S. G., Kessel, R. L., Sibeck, D. G., & Ukhorskiy, A. (2013, November). Science Objectives and Rationale for the Radiation Belt Storm Probes Mission. *Space Science Reviews*, *179*(1-4), 3–27. Retrieved from http://link.springer.com/10.1007/s11214-012-9908-y doi: 10.1007/s11214-012-9908-y

Millan, R. M., Ripoll, J., Santolík, O., & Kurth, W. S. (2021). Early-time non-equilibrium pitch angle diffusion of electrons by whistler-mode hiss in a plasmaspheric plume associated with barrel precipitation. *Frontiers in Astronomy and Space Sciences*, *8*. Retrieved from https://www.frontiersin.org/article/10.3389/fspas.2021.776992 doi: 10.3389/fspas.2021.776992

Morley, S., Niehof, J., Welling, D., Larsen, B., Haiducek, J., Brunet, A., ... Henderson, M. (2021, October). *spacepy/spacepy: 0.2.3.* Zenodo. Retrieved from https://zenodo.org/record/3252523 doi: 10.5281/ZENODO.3252523

Mourenas, D., & Ripoll, J. (2012, January). Analytical estimates of quasi-linear diffusion coefficients and electron lifetimes in the inner radiation belt: ANALYTICAL DIFFUSION COEFFICIENTS. *Journal of Geophysical Research: Space Physics*, *117*(A1). Retrieved from http://doi.wiley.com/10.1029/2011JA016985 doi: 10.1029/2011JA016985

Ozhogin, P., Tu, J., Song, P., & Reinisch, B. W. (2012, June). Field-aligned distribution of the plasmaspheric electron density: An empirical model derived from the IMAGE RPI measurements: EMPIRICAL MODEL OF THE PLASMASPHERE. *Journal of Geophysical Research: Space Physics*, *117*(A6), n/a–n/a. Retrieved from http://doi.wiley.com/10.1029/2011JA017330 doi: 10.1029/2011JA017330

Pedregosa, F., Varoquaux, G., Gramfort, A., Michel, V., Thirion, B., Grisel, O., ... Duchesnay, E. (2011). Scikit-learn: Machine learning in Python. *Journal of Machine Learning Research*, *12*, 2825–2830.

Picone, J. M., Hedin, A. E., Drob, D. P., & Aikin, A. C. (2002, December). NRLMSISE-00 empirical model of the atmosphere: Statistical comparisons and scientific issues: TECHNIQUES. *Journal of Geophysical Research: Space Physics*, *107*(A12), SIA 15–1–SIA 15–16. Retrieved from http://doi.wiley.com/10.1029/2002JA009430 doi: 10.1029/2002JA009430

Ripoll, J., Chen, Y., Fennell, J. F., & Friedel, R. H. W. (2015). On long decays of electrons in the vicinity of the slot region observed by heo3. *Journal of Geophysical Research: Space Physics*, *120*(1), 460-478. Retrieved from https://agupubs.onlinelibrary.wiley.com/doi/abs/10.1002/2014JA020449 doi: https://doi.org/10.1002/2014JA020449

Ripoll, J., Loridan, V., Denton, M. H., Cunningham, G., Reeves, G., Santolík, O., ... Ukhorskiy, A. Y. (2019, February). Observations and Fokker-Planck Simulations of the L -Shell, Energy, and Pitch Angle Structure of Earth's Electron Radiation Belts During Quiet Times. *Journal of Geophysical Research: Space Physics*, *124*(2), 1125–1142. Retrieved from https://onlinelibrary.wiley.com/doi/abs/10.1029/2018JA026111 doi: 10.1029/2018JA026111

Ripoll, J., Santolík, O., Reeves, G. D., Kurth, W. S., Denton, M. H., Loridan, V., ... Turner, D. L. (2017). Effects of whistler mode hiss waves in March 2013. *Journal of Geophysical Research: Space Physics*, *122*(7), 7433–7462. Retrieved from https://onlinelibrary.wiley.com/doi/abs/10.1002/2017JA024139 doi: 10.1002/2017JA024139

Santolík, O., Parrot, M., & Lefeuvre, F. (2003, February). Singular value decomposition methods for wave propagation analysis: SVD METHODS FOR WAVE PROPAGATION ANALYSIS. *Radio Science*, *38*(1). Retrieved from http://doi.wiley.com/10.1029/2000RS002523 doi: 10.1029/2000RS002523

Schulz, M., & Lanzerotti, L. J. (1974). *Particle Diffusion in the Radiation Belts* (Vol. 7; J. G. Roederer, Ed.). Berlin, Heidelberg: Springer Berlin Heidelberg. Retrieved from http://link.springer.com/10.1007/978-3-642-65675-0 doi: 10.1007/978-3-642-65675-0

Selesnick, R. S. (2012, August). Atmospheric scattering and decay of inner radiation belt electrons: INNER RADIATION BELT. *Journal of Geophysical Research: Space Physics*, *117*(A8), n/a–n/a. Retrieved from http://doi.wiley.com/10.1029/2012JA017793 doi: 10.1029/2012JA017793

Shprits, Y. Y., Li, W., & Thorne, R. M. (2006). Controlling effect of the pitch angle scattering rates near the edge of the loss cone on electron lifetimes. *Journal of Geophysical Research: Space Physics*, *111*(A12). Retrieved from https://agupubs.onlinelibrary.wiley.com/doi/abs/10.1029/2006JA011758 doi:

https://doi.org/10.1029/2006JA011758

Tange, O. (2018). *Gnu parallel 2018*. Ole Tange. Retrieved from `https://doi.org/10.5281/zenodo.1146014` doi: 10.5281/zenodo.1146014

Tu, W., Cunningham, G. S., Chen, Y., Henderson, M. G., Camporeale, E., & Reeves, G. D. (2013, October). Modeling radiation belt electron dynamics during GEM challenge intervals with the DREAM3D diffusion model: MODELING RADIATION BELT WITH DREAM3D. *Journal of Geophysical Research: Space Physics*, *118*(10), 6197–6211. Retrieved from `http://doi.wiley.com/10.1002/jgra.50560` doi: 10.1002/jgra.50560

Tu, W., Cunningham, G. S., Chen, Y., Morley, S. K., Reeves, G. D., Blake, J. B., ... Spence, H. (2014, March). Event-specific chorus wave and electron seed population models in DREAM3D using the Van Allen Probes: Tu et al.: Event-specific chorus and seed electrons. *Geophysical Research Letters*, *41*(5), 1359–1366. Retrieved from `http://doi.wiley.com/10.1002/2013GL058819` doi: 10.1002/2013GL058819

Van Allen, J. A. (1964). Lifetimes of Geomagnetically Trapped Electrons of Several Mev Energy. *Nature*, *203*(4949), 1006–1007. Retrieved from `https://www.nature.com/articles/2031006a0` doi: 10.1038/2031006a0

Welch Jr., J. A., Kaufmann, R. L., & Hess, W. N. (1963). Trapped electron time histories for L = 1.18 to L = 1.30. *Journal of Geophysical Research (1896-1977)*, *68*(3), 685–699. Retrieved from `https://onlinelibrary.wiley.com/doi/abs/10.1029/JZ068i003p00685` doi: 10.1029/JZ068i003p00685

West Jr., H. I., & Buck, R. M. (1976). A study of electron spectra in the inner belt. *Journal of Geophysical Research (1896-1977)*, *81*(25), 4696–4700. Retrieved from `https://onlinelibrary.wiley.com/doi/abs/10.1029/JA081i025p04696` doi: 10.1029/JA081i025p04696